WILEY

Geostationary debris mitigation using minimum time solar sail trajectories with eclipse constraints

Patrick Kelly | Riccardo Bevilacqua

Department of Mechanical and Aerospace Engineering, University of Florida, Gainesville, Florida

Correspondence
Patrick Kelly, Department of Mechanical and Aerospace Engineering, University of Florida, Gainesville, FL, USA.
Email: pkelly89@ufl.edu

Summary

Minimum time solar sailing trajectories are introduced using a combination of indirect and direct optimal control techniques. Here, large-scale, multiphase optimal control problems are solved using a pseudospectral collocation technique applied to an orbital debris mitigation concept. These solutions are obtained for realistic sail dimensions, producing multirevolution, Earth-centered trajectories while accounting for uncontrolled spacecraft dynamics in the eclipse regions. Specifically, minimum time solutions for orbit transfer and phasing maneuvers are obtained using only solar radiation pressure for propulsion and control. First, an optimal primer vector steering history is obtained through numerical approximation. Locally optimal, closed-form solutions are then implemented based on the primer vector direction, resulting in minimum time satisfaction of desired terminal orbital conditions. In addition, a novel solution strategy is presented for multiphase optimal control problems characterized by uncontrollable dynamics with flexible phase boundaries. The maneuvers presented will be shown to enable efficient orbital debris mitigation for large-scale debris in geostationary orbits.

KEYWORDS
eclipsing, orbital debris, solar sail, trajectory optimization

1 | INTRODUCTION

Solar sailing provides a propellantless propulsion solution for satellite maneuvering. Here, thrusting capabilities are generated from solar radiation pressure (SRP), utilizing the momentum exchange between photons and the sun-exposed surfaces of a spacecraft. The resulting forces acting upon the spacecraft can be utilized for continuous low-thrust (CLT) maneuvering. In practice, solar sailing spacecraft must employ large, lightweight, highly reflective surfaces, and exhibit very low-thrust capabilities. For a spacecraft with a typical surface area to mass ratio on the order of 0.01 $\frac{m^2}{kg}$,[1] the resulting SRP acceleration is less than 10^{-10} $\frac{km}{s^2}$. To achieve propulsive capabilities comparable to conventional low-thrust systems, a solar sailing spacecraft would require an area to mass ratio closer to 10 $\frac{m^2}{kg}$. Between the growing popularity (and capability) of CubeSats and the wealth of research regarding CLT spacecraft maneuvering,[2-6] solar sailing is only recently becoming a plausible means of spacecraft propulsion.

Practical use of solar sailing has been validated through JAXA's *IKAROS* spacecraft in 2010.[7] The Planetary Society has launched *LightSail 2*,[8] a 32 m² sail on a 3U platform. Additional solar sailing concepts are being developed, and help frame the current state-of-the-art in solar sailing capabilities: NASA's *Near-Earth Asteroid (NEA) Scout* is a 86 m² concept on a

6U platform.[9] To obtain an understanding of the upper bounds of solar sail development, NASA's *Sunjammer* spacecraft boasts a sail surface area of approximately 1200 m^2.[10] Using these examples, feasible sail trajectories can be developed based on real-life sail dimensions to motivate additional solar sailing applications in the near future. In particular, orbital debris mitigation can be addressed for high-altitude orbits where atmospheric drag is not an actor. Using a solar sail, large-scale orbital debris may be removed from geostationary orbits (GEO) and placed into a retirement orbit as defined by the Inter-Agency Space Debris Coordination Committee (IADC).[11,12] The IADC deorbit guidelines are provided in Tables B1 and B2 in the appendix. Generally, a deorbit maneuver from the geostationary belt requires a raise in altitude greater than 235 km into a near circular final orbit beyond the space of operating spacecraft. Though many satellites are launched with varying levels of deorbit capability, unforeseen systems failures threaten the likelihood of successful deorbit at end-of-life.[13-15] Using a solar sail, unresponsive satellites and rocket bodies can be removed from the geostationary region, repeatably, using free propulsion.

Solar sail maneuvers are marked by very low-thrust propulsion, resulting in maneuvers of long-duration and many revolutions for planet-centered applications. Furthermore, unique physical constraints require the spacecraft to be exposed to the sun and allow SRP accelerations only in outward directions from the sun. Recent investigations into SRP trajectory optimization have been focused primarily on applications involving restricted three body problems or interplanetary trajectory optimization. Fekete[16] and Pagel[17] determined sail trajectories from the Earth to the moon. Optimized sail trajectories in the Earth-Moon system are additionally obtained by Howell[18] and Wawrzyniak.[19] Optimal sail trajectories to the outer solar system have been investigated by Dachwald.[20] More recently, the automated trajectory optimizer for solar sailing has been developed for trajectory design for sail propelled planetary transfers or NEA rendezvous by Peloni et al[21,22] Locally optimal solutions have been obtained for planet-centered orbits but do not account for eclipsing or high-fidelity dynamics models.[23-30] Ultimately, none of these works address the specific challenges of Earth-centered orbit transfer and phasing maneuvering using realizable sail-system masses or dimensions. In addition, eclipsing phenomena have not been handled directly.

In this study, geostationary deorbit and rendezvous solar sailing trajectories will be obtained in minimum time while addressing eclipsing phenomena. Control of the spacecraft trajectory is only possible during illumination phases. During eclipse phases, the spacecraft orbits freely under the influence of multiple gravitational disturbances, creating discontinuities in the control histories. Maneuvering solutions are obtained by subdividing the spacecraft trajectory into multiple phases, alternating between illuminated and eclipsed states in a similar manner as previous works.[3,5] The proposed maneuvers will support the *TugSat* concept where a small satellite is tasked with repeatedly deorbiting large orbital debris from the GEO belt using SRP propulsion.[31,32] The TugSat mission involves a deorbit segment and a phasing segment. The deorbit segment relies on trajectories which relocate large orbital debris into a disposal, or *graveyard*, orbit as defined by the parameters in Table B2. During the phasing segment, the sail-craft must return from the graveyard regime to a specific equatorial longitude in the GEO belt for rendezvous with a new payload. Definitions for the GEO belt dimensions for the return orbit are provided in Table B1.

The TugSat orbital debris migitation concept, as first introduced in Kelly et al,[31] would achieve successful deorbit to the graveyard regime and return to the protected geostationary region through manipulation of key orbital elements in careful sequence. The deorbit maneuver was shown achievable in 220 days while the return maneuver would occur anywhere between 180 days to over 10 years. Deorbit times are improved for various sail sizes in Kelly and Bevilacqua,[32] where a closed-form sail maneuvering strategy is introduced and optimized heuristically using particle swarm optimization, ultimately reducing deorbit times by over 20%. In this work, deorbit times are further improved by steering the direction of the primer vector presented in Kelly and Bevilacqua,[32] and implementing sail orientations based on the closed-form solution. Deorbit maneuvers will be obtained which occur on the order of 90 days. In addition, minimum time orbit phasing solutions will place the sail-craft within a desired GEO belt longitude in under 60 days.

To obtain the minimum time maneuvering solutions which follow, a direct collocation method is employed. Specifically, an iterative collocation scheme utilizing adaptive mesh refinement is executed using GPOPS-II.[33] Here, the collocation method is a Gaussian quadrature implicit integration method with collocation applied at Legendre-Gauss-Radau (LGR) points.[34-36] The adaptive mesh-refinement procedure is a *ph* mesh refinement method described in Patterson et al[37] First derivative approximations are performed using a sparse finite-differencing method from Patterson and Rao.[38] The solver employed is SNOPT, a sparse nonlinear programming (NLP) software package for large-scale nonlinear optimization.[39,40] First, minimum time solutions for deorbit from and rephasing to the GEO belt are obtained without eclipsing. These solutions are postprocessed to determine the approximate location of eclipsing events for setup of a multiple phase optimal control problem. With these events in place, an updated minimum time solution is then obtained which accounts for sail transits through uncontrollable shadow regions. The resulting trajectories are realizable given

contemporary solar sailing practices and demonstrate the heightened possibilities of solar sailing small satellites. What follows is the first application of orthogonal collocation techniques to obtain numerically optimized, planetocentric solar sailing trajectories with eclipsing.

Specifically, contributions to the state-of-the-art in this work include:

- Numerically optimized primer vector histories to generate closed-form sail orientations
- Minimum time deorbit and phasing solutions using SRP propulsion with contemporary sail dimensions
- Eclipse event determination via accurate approximation from non-eclipse solutions
- High-fidelity orbit propagation strategy for multiphase optimal control problems with flexible phase boundaries

The remainder of this discussion is organized as follows. Section 2 describes the equations of motion and disturbance forces in the dynamic modeling. Section 3 expands on the unique constraints and considerations involved with utilizing a solar sail for controlled maneuvering. Section 4 introduces and outlines the methods used to set up the solution structure to the solar sailing optimal control problem. Section 5 transcribes the deorbit and phasing problems into an NLP and provides minimum time solutions for eclipsed solar sail trajectories. The summary of major outcomes are summarized in Section 6. Constants and useful definitions are provided in the appendix.

2 | DYNAMIC MODELING

The equations of motion describing a perturbed spacecraft orbit about the Earth ($\oplus$) are expressed in an inertially fixed reference frame as

$$\ddot{\boldsymbol{r}} + \frac{\mu_\oplus}{r^3}\boldsymbol{r} = \boldsymbol{a}_d, \tag{1}$$

where $\boldsymbol{r}$ is the spacecraft's position vector of magnitude r and $\boldsymbol{a}_d$ is the disturbance acceleration acting upon the spacecraft. Here, the disturbance acceleration is composed of contributions from Earth's nonuniform mass distribution, third body effects from the moon and sun, and a nongravitational disturbance from SRP. In this study, accelerations are resolved in an Earth-centered, inertial (*ECI*) coordinate system, defined with the primary axis ($\hat{\boldsymbol{I}}$) pointing in the direction of the vernal equinox, tertiary axis ($\hat{\boldsymbol{K}}$) assumed aligned with the Earth's north pole, and secondary axis ($\hat{\boldsymbol{J}}$) completing the right-handed basis. An Earth-centered, Earth-fixed (*ECEF*) coordinate system is defined on a rotating reference frame with origin at the center of mass of the Earth and axes aligned with the Earth's principal axes of inertia. In this manner, the fundamental plane $\hat{\bar{\boldsymbol{x}}}$-$\hat{\bar{\boldsymbol{y}}}$ contains the Earth's equator and rotates about $\hat{\bar{\boldsymbol{z}}} = \hat{\boldsymbol{K}}$ at a rate of $\omega_\oplus$ as defined in the appendix. Finally, the local-vertical, local-horizontal (*LVLH*) coordinate system is defined on the spacecraft orbit reference frame using basis vectors $\{\hat{\boldsymbol{r}},\ \hat{\boldsymbol{s}},\ \hat{\boldsymbol{w}}\}$ obtained geometrically through

$$\hat{\boldsymbol{r}} = \frac{\boldsymbol{r}}{r}, \tag{2a}$$

$$\hat{\boldsymbol{w}} = \frac{\boldsymbol{r} \times \boldsymbol{v}}{\|\boldsymbol{r} \times \boldsymbol{v}\|}, \tag{2b}$$

$$\hat{\boldsymbol{s}} = \hat{\boldsymbol{w}} \times \hat{\boldsymbol{r}}, \tag{2c}$$

where $\boldsymbol{v}$ is the spacecraft velocity vector relative to the inertial frame. Figure 1 illustrates the relationship between these coordinate systems. Specific values for the physical parameters to follow are provided in Tables A1 and A2 within the appendix.

2.1 | Disturbance forces

The aspherical potential field used in this model accounts for second-order gravitational disturbances[41] and is defined as

$$U = \frac{\mu_\oplus}{r}\left(\frac{R_\oplus}{r}\right)^2\left[3\Gamma_{22}\frac{r_{\bar{x}}^2 - r_{\bar{y}}^2}{r^2} - \frac{1}{2}\Gamma_{20}\left(1 - 3\frac{r_{\bar{z}}^2}{r^2}\right)\right], \tag{3}$$
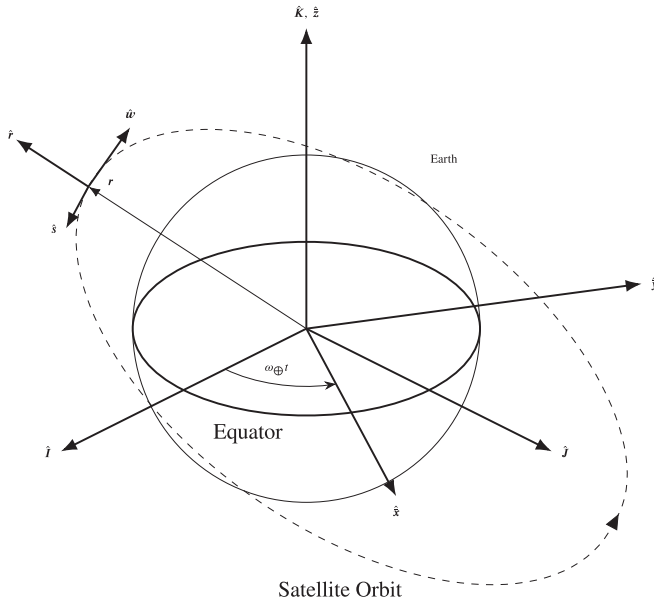
FIGURE 1 Earth-based coordinate system relationships for *ECI* $\{\hat{I}, \hat{J}, \hat{K}\}$, *ECEF* $\{\hat{\bar{x}}, \hat{\bar{y}}, \hat{\bar{z}}\}$, and *LVLH* $\{\hat{r}, \hat{s}, \hat{w}\}$

where $\{r_{\bar{x}},\ r_{\bar{y}},\ r_{\bar{z}}\}$ are the spacecraft coordinates in the *ECEF* coordinate system, $R_\oplus$ is the mean equatorial radius of the Earth, and Γ_{20} and Γ_{22} are the normalized harmonic coefficients defined as

$$\Gamma_{20} \simeq C_{20}, \tag{4a}$$

$$\Gamma_{22} \simeq \sqrt{C_{22}^2 + S_{22}^2}. \tag{4b}$$

Numerical values for $R_\oplus$, Γ_{20}, and Γ_{22} are provided in the appendix. The disturbance acceleration resulting from Equation (3) is obtainable from

$$\boldsymbol{a}_\oplus = \nabla U. \tag{5}$$

Notice, a coordinate transformation is required to resolve Equation (5) in the *ECI* coordinate system. This transformation has been applied for all numerical calculations in this work.

The disturbance force from a neighboring celestial body, n, is accounted for in an inertially fixed reference frame using

$$\boldsymbol{a}_n = \mu_n \left(\frac{\boldsymbol{r}_{\text{sat},n}}{r_{\text{sat},n}^3} - \frac{\boldsymbol{r}_{\oplus,n}}{r_{\oplus,n}^3} \right), \tag{6}$$

where $\boldsymbol{r}_{i,j} \triangleq \boldsymbol{r}_i - \boldsymbol{r}_j$. To minimize numerical errors known to exist in Equation (6), the following substitution is used[42]

$$\frac{\boldsymbol{r}_{\text{sat},n}}{r_{\text{sat},n}^3} - \frac{\boldsymbol{r}_{\oplus,n}}{r_{\oplus,n}^3} = Q\,\boldsymbol{r}_{\text{sat},n} - \frac{\boldsymbol{r}_{\oplus,\text{sat}}}{r_{\oplus,n}^3}, \tag{7}$$

where

$$Q = \frac{(r_{\oplus,\text{sat}}^2 + 2\,\boldsymbol{r}_{\oplus,\text{sat}} \cdot \boldsymbol{r}_{\text{sat},n})(r_{\oplus,n}^2 + r_{\oplus,n}r_{\text{sat},n} + r_{\text{sat},n}^2)}{r_{\oplus,n}^3\, r_{\text{sat},n}^3\, (r_{\oplus,n} + r_{\text{sat},n})} \tag{8}$$

resulting in the numerically stable expression

$$\boldsymbol{a}_n = \mu_n \left(Q \, \boldsymbol{r}_{\text{sat},n} - \frac{\boldsymbol{r}_{\oplus,\text{sat}}}{r_{\oplus,n}^3} \right). \tag{9}$$

Equation (9) is applied in this study to capture gravitational disturbances from the sun ($\odot$) and moon ($\mathbb{C}$). SRP is the lone nongravitational perturbation in this dynamics model and is expressed as Reference 43

$$\boldsymbol{a}_{\text{SRP}} = -\kappa P_\odot \frac{\text{AU}^2}{r_\odot^2} \frac{A}{m} \cos\theta [(1-\varepsilon)\hat{\boldsymbol{e}}_\odot + 2\varepsilon \cos\theta \hat{\boldsymbol{n}}] \tag{10}$$

with SRP $P_\odot$, shadow coefficient κ (for occultations from the moon and the Earth), astronomical unit AU, sail surface area to mass ratio $\frac{A}{m}$, reflectivity coefficient ε, sun direction unit vector $\hat{\boldsymbol{e}}_\odot$, which points in the direction of the sun, relative to the satellite's center of mass, and the sun-sail angle θ, obtained from

$$\cos\theta \triangleq \hat{\boldsymbol{e}}_\odot \cdot \hat{\boldsymbol{n}}, \quad \theta \in \left[0, \frac{\pi}{2}\right] \tag{11}$$

with bounds constraining $\hat{\boldsymbol{n}}$ to point "towards" the sun. Sail trajectories in this work assume a perfectly reflective sail surface, such that $\varepsilon \triangleq 1$. The shadow coefficient takes on values $\kappa \in [0, 1]$, where $\kappa = 1$ corresponds to a fully illuminated sail-craft and $\kappa = 1$ is fully eclipsed. For solar sailing applications, the control ($\mathbf{u}$) is captured in $\mathbf{a}_{\text{SRP}}$, typically through selection of $\hat{\mathbf{n}}$ (ie, $\mathbf{u} = \hat{\mathbf{n}}$).

The total disturbance acceleration is the sum of these perturbations

$$\boldsymbol{a}_d = \boldsymbol{a}_\oplus + \boldsymbol{a}_\mathbb{C} + \boldsymbol{a}_\odot + \boldsymbol{a}_{\text{SRP}}. \tag{12}$$

To obtain $\boldsymbol{a}_d$ in the analysis to follow, sun and moon ephemeris dependencies are resolved using analytical approximations based on Julian date inputs.[44]

2.2 | Dynamics

The dynamics of a spacecraft in response to the disturbance accelerations can be modeled in Gaussian form using modified equinoctial orbital elements (MEOE), defined as

$$p \triangleq a(1 - e^2), \tag{13a}$$

$$f \triangleq e\cos(\Omega + \omega), \tag{13b}$$

$$g \triangleq e\sin(\Omega + \omega), \tag{13c}$$

$$\hbar \triangleq \tan\left(\frac{i}{2}\right)\cos(\Omega), \tag{13d}$$

$$k \triangleq \tan\left(\frac{i}{2}\right)\sin(\Omega), \tag{13e}$$

$$L \triangleq \Omega + \omega + \nu, \tag{13f}$$

where $\{a, e, i, \Omega, \omega, \nu\}$ is the classical orbital element (COE) set. Using Equation (13), the state is defined $\mathbf{x} = [p, f, g, \hbar, k, L]^\top$ with associated dynamics of the form

$$\dot{\mathbf{x}} = \mathbf{ZF} + \mathbf{b} = \mathbf{f}(\mathbf{x}, \mathbf{u}, t), \tag{14}$$

where

$$\mathbf{Z} = \frac{1}{q}\sqrt{\frac{p}{\mu}}\begin{bmatrix} 0 & \frac{2p}{q} & 0 \\ q\sin L & (q+1)\cos L + f & -g(\hbar\sin L - k\cos L) \\ -q\cos L & (q+1)\sin L + g & f(\hbar\sin L - k\cos L) \\ 0 & 0 & \frac{\varsigma^2\cos L}{2} \\ 0 & 0 & \frac{\varsigma^2\sin L}{2} \\ 0 & 0 & \hbar\sin L - k\cos L \end{bmatrix} \tag{15}$$

and

$$\mathbf{b} = \begin{bmatrix} 0 & 0 & 0 & 0 & 0 & \sqrt{\mu p}\left(\frac{q}{p}\right) \end{bmatrix}^{\mathsf{T}} \tag{16}$$

using definitions

$$q \triangleq 1 + f\cos L + g\sin L, \tag{17a}$$

$$\varsigma^2 \triangleq 1 + \hbar^2 + k^2. \tag{17b}$$

From these definitions, the orbital radius is readily obtained using $r = \frac{p}{q}$. For the Earth-centered maneuvers in this work, $\mu = \mu_\oplus$ is used and the specific force $\mathbf{F}$ in Equation (14) is equivalent to the disturbance acceleration $\boldsymbol{a}_d$, from Equation (12), expressed mathematically using *LVLH* components through

$$\mathbf{F} = \mathbf{C}^{\mathsf{T}}\boldsymbol{a}_d, \tag{18a}$$

$$= [F_r \quad F_s \quad F_w]^{\mathsf{T}}, \tag{18b}$$

where

$$\mathbf{C} \triangleq [\hat{\mathbf{r}} \quad \hat{\mathbf{s}} \quad \hat{\mathbf{w}}] \tag{19}$$

is a direction cosine matrix which transforms coordinates from the *LVLH* coordinate system to the *ECI* coordinate system using the basis vector definitions provided in Equation (2). Control is introduced into Equation (18) through proper selection of $\hat{\mathbf{n}}$ as detailed in Section 3.

2.3 | Change of variable

For long duration simulations, it is often beneficial to integrate the dynamics in terms of true longitude instead of time.[3-5] Assuming prograde orbiting solutions, L is monotonically increasing and is a suitable independent variable substitute for time. Specifically, integrating the dynamics in terms of L helps to locate eclipse terminator points for the multiphase optimal control problem. During the optimization process, these terminator locations may differ greatly in terms of time and can prevent solutions from varying too far from a supplied initial guess. Regardless of time, however, the spacecraft experiences eclipsing phenomena in relatively similar locations in L for all solutions initialized at a common epoch. From Equations (15) and (16), the change in true longitude with respect to time is

$$\frac{dL}{dt} = \frac{1}{q}\sqrt{\frac{p}{\mu}}(\hbar\sin L - k\cos L)F_w + \sqrt{\mu p}\left(\frac{q}{p}\right)$$
$$= f_L(\mathbf{x}, \mathbf{u}, t) \tag{20}$$

allowing for

$$t' = \frac{dt}{dL} = \frac{1}{f_L(\mathbf{x}, \mathbf{u}, t)}. \tag{21}$$

The change of variable can be carried out for the remaining MEOE expressions using

$$p' = t' \cdot f_p(\mathbf{x}, \mathbf{u}, t), \tag{22a}$$

$$f' = t' \cdot f_f(\mathbf{x}, \mathbf{u}, t), \tag{22b}$$

$$g' = t' \cdot f_g(\mathbf{x}, \mathbf{u}, t), \tag{22c}$$

$$\hbar' = t' \cdot f_h(\mathbf{x}, \mathbf{u}, t), \tag{22d}$$

$$k' = t' \cdot f_k(\mathbf{x}, \mathbf{u}, t). \tag{22e}$$

The updated state is now $\mathbf{x} = [p, \ f, \ g, \ \hbar, \ k, \ t]^{\mathsf{T}}$ with dynamics $\mathbf{x}' = \mathbf{f}(\mathbf{x}, \mathbf{u}, L)$.

3 | SOLAR SAILING

3.1 | Solar sail control

Solar sail control is made possible through user selection of the sail pointing vector $\hat{\mathbf{n}}$. Closed-form expressions for locally optimal sail orientations are known to exist, which produce extremal rates of change for a desired orbital parameter.[26] It has been shown by Kelly and Bevilacqua[32] that the SRP response can be optimized with respect to some primer vector $\boldsymbol{\zeta}$. Physically, $\boldsymbol{\zeta}$ can be defined as the dynamic constraint vector corresponding to the rate of change in a specified orbital parameter such as ξ (specific orbital energy), a, or e. More generally, $\boldsymbol{\zeta}$ defines the dynamic response, due to SRP, across a specified direction and is an instance of the primer vector.[45] For example, to maximize p', the associated constraint vector obtained from Equation (15) would have *LVLH* components defined $\boldsymbol{\zeta}_p = t' \cdot \left[0 \ \frac{2p}{q} \ 0\right]^{\mathsf{T}} \forall L$. Figure 2 illustrates the relationship between $\hat{\mathbf{n}}$, $\hat{\boldsymbol{\zeta}}$, and $\hat{\mathbf{e}}_\odot$. Here, the basis vectors are defined as

$$\hat{\mathbf{e}}_1 = \hat{\mathbf{e}}_\odot, \tag{23a}$$

$$\hat{\mathbf{e}}_3 = \frac{\hat{\mathbf{e}}_\odot \times \boldsymbol{\zeta}}{\|\hat{\mathbf{e}}_\odot \times \boldsymbol{\zeta}\|}, \tag{23b}$$

$$\hat{\mathbf{e}}_2 = \hat{\mathbf{e}}_3 \times \hat{\mathbf{e}}_1. \tag{23c}$$

The sail angles α and β are sail yaw and pitch control angles, respectively, and the angle γ is the primer vector angle measured from $\hat{\mathbf{e}}_\odot$ to $\boldsymbol{\zeta}$.

From Kelly and Bevilacqua,[32] locally optimal sail angles are given as

$$\alpha^\star = \tan^{-1}\left(\frac{-3\cos\gamma + \sqrt{\cos^2\gamma + 8}}{4\sin\gamma}\right) \quad \in \left[0, \ \frac{\pi}{2}\right], \tag{24a}$$

$$\beta^\star = 0. \tag{24b}$$

In instances where a specific orbital parameter rate is to be optimized, $\boldsymbol{\zeta}$ is always defined and γ is necessarily uncontrollable as $\hat{\mathbf{e}}_\odot$ and $\boldsymbol{\zeta}$ uniquely define the $\{\hat{\mathbf{e}}_1, \ \hat{\mathbf{e}}_2, \ \hat{\mathbf{e}}_3\}$ basis. In addition, with $\{\alpha^\star, \beta^\star\}$ defined, the sail system will orient deterministically, achieving locally optimal SRP contributions to maximize the rate of change associated with the given
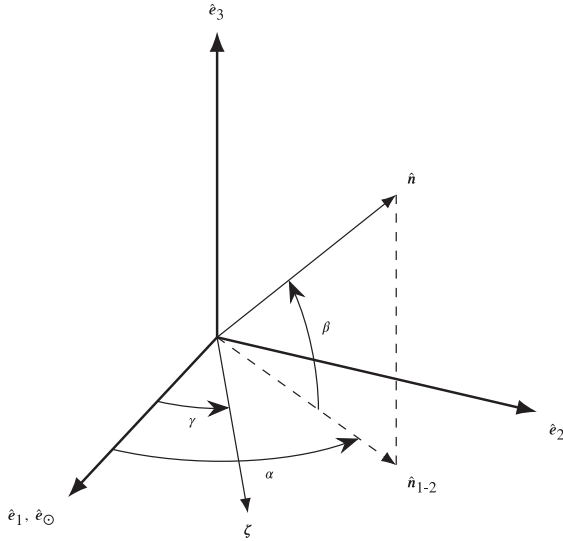
FIGURE 2 Sail orientation $\hat{n}$, along with planar projection $\hat{n}_{1-2}$, expressed in basis formed between sun direction vector $\hat{e}_\odot$ and primer vector ζ

ζ. In this study, however, $\hat{\zeta}$ is treated as the control input, corresponding to a primer vector whose direction and composition are not known a priori. In this manner, the objective is to determine the optimal primer vector pointing history which produces γ angles associated with minimum time deorbit or phasing trajectories. Control variables in this problem transcription are then the components of the primer unit vector, defined as

$$\mathbf{u} = \frac{1}{\|\zeta\|} [\ \zeta_r\ \zeta_s\ \zeta_w\ ]^\mathsf{T} = [\ u_r\ u_s\ u_w]^\mathsf{T}. \tag{25}$$

Now, as $\mathbf{u}$ represents a unit vector, the control vector magnitude must equal unity. This reduces the dimensionality of the unknown control variables, resulting in the path constraint

$$u_r^2 + u_s^2 + u_w^2 = 1. \tag{26}$$

Using this strategy, control of $\hat{n}$ is achieved through approximation of the primer vector direction, rather than through direct approximation of $\{\alpha^\star, \beta^\star\}$.

3.2 | Eclipse handling

Solar sailing applications require direct exposure to sunlight for propulsion. In practice, a planet-centered sail-craft will encounter eclipsing events due to occultations by the moon and Earth. During penumbral transits, the space-craft is exposed to some fraction of the maximum available sunlight while during umbral transits, the spacecraft is completely eclipsed by the occulting body. Due to the vast distances between the sun and occulting bodies, it is reasonable to assume the amount of time spent in penumbra is negligible compared with the amount of time spent in umbra. For the purposes of this research, the spacecraft is assumed to be completely eclipsed even during the penumbral phases. In addition, occultation events caused by the moon are considered to be negligible due to the brief duration and infrequent number of sun-moon eclipsing events. To locate relevant eclipsing events, a conical shadow model is used to determine the illumination status of the spacecraft as shown in Figure 3.[46] Here, the illuminating body is the sun of radius $R_\odot$, and is occulted by the Earth, of radius $R_\oplus$. The apex, P, of the resulting penumbral cone lies along a shadow axis connecting the sun and Earth at a distance d_p from the center of the Earth

$$d_p = \frac{R_\oplus\ d_\odot}{R_\odot + R_\oplus}. \tag{27}$$

FIGURE 3 Conical eclipse model
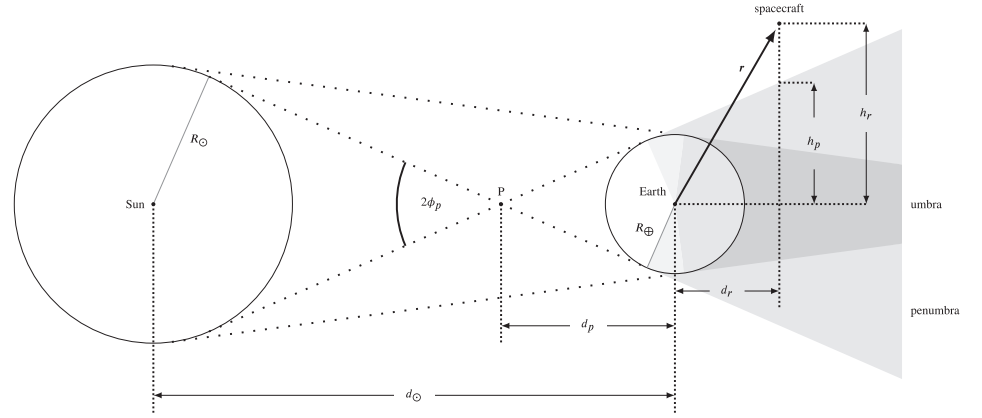
The distance $d_\odot$ is measured between the centers of the sun and Earth. A penumbra cone angle, denoted ϕ_p, can now be defined

$$\phi_p = \arcsin\left(\frac{R_\oplus}{d_p}\right) = \arcsin\left(\frac{R_\odot + R_\oplus}{d_\odot}\right). \tag{28}$$

To determine the illumination status of the spacecraft, the position vector $\boldsymbol{r}$ is polled in relation to a unit vector $\hat{\boldsymbol{r}}_\odot$ pointing from the Earth to the sun. The spacecraft position vector projected onto the shadow axis is

$$\bar{\boldsymbol{r}} = (\boldsymbol{r} \cdot \hat{\boldsymbol{r}}_\odot)\hat{\boldsymbol{r}}_\odot. \tag{29}$$

A distance parameter d_r, measured along $\hat{\boldsymbol{r}}_\odot$, is defined as

$$d_r \triangleq \|\bar{\boldsymbol{r}}\|. \tag{30}$$

The orthogonal distance between the spacecraft and the shadow axis can be obtained through

$$h_r = \|\boldsymbol{r} - \bar{\boldsymbol{r}}\|. \tag{31}$$

Now, the penumbra terminator point associated with the current spacecraft position $\boldsymbol{r}$ is located orthogonal to the shadow axis at a distance h_p defined

$$h_p = (d_p + d_r)\tan\phi_p. \tag{32}$$

Ultimately, a spacecraft is located within the penumbra cone when the following condition is satisfied:

$$\theta_r \leq \theta_p \tag{33}$$

with polar angle definitions

$$\theta_p = \tan^{-1}\left(\frac{h_p}{d_r}\right), \quad \in \left[0, \frac{\pi}{2}\right], \tag{34}$$

$$\theta_r = \tan^{-1}\left(\frac{h_r}{\boldsymbol{r} \cdot \hat{\boldsymbol{r}}_\odot}\right), \quad \in [0, \pi]. \tag{35}$$

The spacecraft resides exactly on the termination point of the penumbra region when $\theta_r = \theta_p$.

In practice, spacecraft in the GEO region are subject to eclipsing events twice per year, when the Earth-sun geometry lies about the vernal equinox line (ie, during the vernal and autumnal equinoxes). Outside of these equinoctial regions, the obliquity of the ecliptic keeps the GEO belt fully illuminated by the sun.

4 | OBTAINING MINIMUM TIME SOLUTIONS

Special care must be taken when structuring the initial guess for the NLP solver in order to produce a feasible solution. For spacecraft trajectory optimization problems, approximations of thrust arcs and short term oscillations in the orbital elements may exhibit general solution profiles which repeat roughly once per orbit. With this in mind, initial mesh structures here are subdivided into equally spaced intervals based on the number of revolutions associated with the initial guess of the solution. Specifically, multiple revolution trajectories are initially defined using one mesh interval per revolution with an equal number of collocation points within each mesh interval. In the discussion to follow, minimum time solar sailing solutions are obtained by first considering trajectories which are assumed to be fully illuminated by the sun at all times. Upon selection of a non-eclipsed, minimum time trajectory, the solution is post-processed to determine the locations of eclipsing events along the candidate trajectory. Based on the locations of these eclipsing events, a new eclipsed trajectory is formed by partitioning the non-eclipsed solution into multiple phases, consisting of alternating illuminated and eclipsed phases. This trajectory serves as an initial guess for the minimum time eclipsing solution. Here, a novel method for obtaining accurate state approximations across eclipse regions will be introduced. This method can be applied to all multiphase optimal control problems which include uncontrollable phases.

4.1 | Non-eclipsed maneuvers

The transcription of the minimum time solar sailing problem requires definitions of bounds on the state, control, and constraint space as well as the supply of an initial guess of the state and control trajectories. Defining the bounds on the solution space can be performed based on knowledge of the spacecraft dynamics and orbital mechanics; however, determination of a suitable initial guess proves more challenging. It is well known that candidate solutions for the trajectory optimization problem often lie within a close neighborhood to that of the initial guess.[3,4] Difficulty arises in generating a suitable initial guess without introducing excessive biasing on the solution structure. In an effort to prevent such biasing, the transcription method here only considers an initial guess on the state and control histories at the beginning and end of the trajectory (ie, at L_0 and L_f). Most importantly, the solution biasing here was observed to be overwhelmingly dependent upon the initial guesses on variables t_f and L_f. Candidate solutions frequently converged to within ± 1 day of an initially supplied estimate of the final time and $\pm 2\pi$ of an initially supplied estimate of the final true longitude. To address this phenomenon, an iterative search method is employed.

As all maneuvers take place within a close proximity of the GEO belt, it is reasonable to assume the final number or revolutions associated with the optimal trajectory will approximately equal the final number of days it takes to complete the maneuver. Denoting $\tilde{L}_f$ and $\tilde{t}_f$ the initial guesses on the final true longitude and time, respectively, the integer N is introduced where $\tilde{L}_f = N$ revs and $\tilde{t}_f = N$ days. Starting with an initial guess of N, an optimal solution candidate is sought. Once a solution is initially obtained, N is reduced by one and a new candidate solution is sought. When N can be reduced no further to obtain a solution, the trajectory associated with the smallest N value is deemed the minimum time solution and the final time associated with the last solution obtained will be denoted $t_f^\star$. This search method is founded upon the observation that for these simulations, any two L_f values $L_{f,i}$ and $L_{f,j}$, where $L_{f,i} < L_{f,j}$, the final times satisfy the behavior $t_{f,i} < t_{f,j}$. To further reduce the risk of solution biasing, the method below allows for the underestimation of N, requiring no a priori knowledge of the expected duration of the minimum time maneuver. The procedure for obtaining the minimum time solution is detailed in Algorithm 1.

Algorithm 1. Minimum time solution procedure

---

1. **Initialization**
    i Define bounds on $\mathbf{x}$, $\mathbf{u}$, and $\mathbf{c}$
    ii Supply initial guess for $\mathbf{x}$ and $\mathbf{u}$ at beginning and end of trajectory
    iii Select value of N
    iv Define solution counter $i_{\text{sol}} = 0$
2. **Optimization**
    i Set $\tilde{L}_f = N \sim$ revs and $\tilde{t}_f = N \sim$ days
    ii Divide mesh into N equally space intervals
    iii Attempt minimum time solution using GPOPS-II with SNOPT
3. **Termination Tests**

    if solution is found **then**

    i Set $i_{\text{sol}} = i_{\text{sol}} + 1$
    ii Set $t_f^\star = t_f$
    iii Set $N = N - 1$ and go back to step 2
    else if $i_{\text{sol}} > 1$ **then**

    i Set $N = N + 5$
    ii Go back to step 2
    else

    i Terminate search algorithm
    ii $t_f^\star$ is minimum time solution
    end if

Specific selections on bounds and initial guess definitions are detailed in Section 5.

4.2 | Eclipsing maneuvers

To obtain more realistic expectations for the optimal deorbit performance, the effects of the penumbral regions must be taken into consideration. Previous works have implemented a receding horizon approach, where a solution to the optimal control problem is obtained and saved up to the first encounter of a penumbra terminator point.[3,5] Upon encounter of an eclipse region, the spacecraft trajectory is assumed to be Keplerian ($\mathbf{a}_d = \mathbf{0}$), where the orbital elements (except for true longitude) are held constant during transits between penumbral terminator points. Estimated values for L can be computed analytically at the terminator points as described in Betts.[47] Once the spacecraft reenters an illuminated region, the optimal control problem is solved once more. The initial conditions are updated, coinciding with reentry into the illuminated region, and the trajectory is saved until the next shadow region is encountered. This sequence repeats until the minimum time solution is obtained. A patched solution, consisting of piecewise fragments of the multiple optimal control solutions, is then used as an initial guess for a multiphase optimal control problem. Figure 4 illustrates the piecewise nature of the multiphase optimal control problem. Phases are linked such that

$$L_f^{(i)} = L_0^{(i+1)} \tag{36}$$

and

$$[\, p \; f \; g \; \hbar \; k \; t \,]_{L_f^{(i)}} = [\, p \; f \; g \; \hbar \; k \; t \,]_{L_0^{(i+1)}}, \tag{37}$$
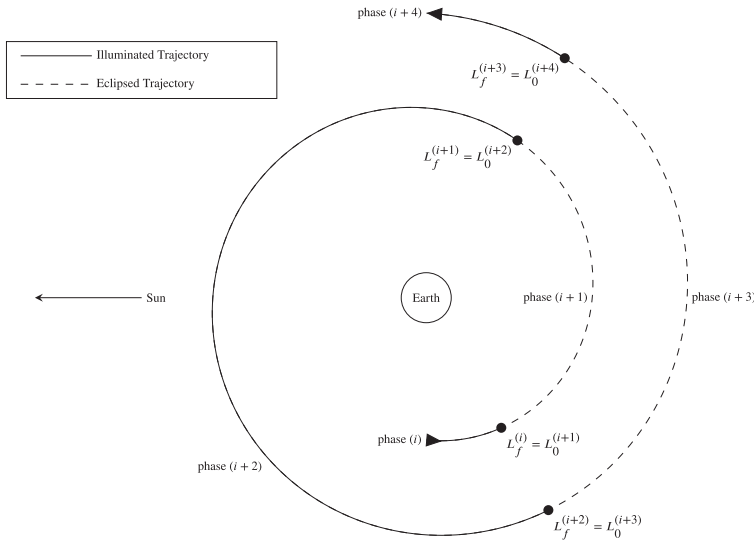
FIGURE 4 Conceptual depiction of the multiphase trajectory resulting from eclipsing phenomena. True longitudes at the junctions between phases are shown to be equal

where the superscript $(i) \in \{1, 2, \ldots, P\}$ denotes the phase number for the multiphase optimal control problem consisting of P phases. This method may be sufficient to obtain an approximate of the minimum time solution, but is inherently unrepresentative of the problem to be solved due to the substitution of oversimplified dynamics across the shadow transit region. The resulting inaccuracies are even more consequential for orbit transfers which exhibit many revolutions across an eclipse region. For scenarios where high accuracy solutions are desired, an alternative solution method must be implemented which maintains the fidelity of the dynamic modeling, even across the eclipse regions.

4.2.1 | Eclipsed trajectory approximation

Here, a novel orbit approximation technique is introduced, which assumes spacecraft motion subject to the same level of dynamic modeling fidelity across the entire orbit transfer. In this formulation, the only difference between an eclipse and an illuminated region is the presence of the control input ($\mathbf{a}_{SRP}$). Consider an eclipse region as modeled in Figure 3. Using Equation (1), the disturbance forces acting on the spacecraft are caused by gravitational perturbations from the Earth's nonspherical mass distribution as well as those from the sun and the moon. It would appear, accurately, that the dynamics from Equation (14) are now uncontrollable as $\mathbf{u}$ is no longer included in the system. Without a control variable, the NLP solver will be unable to determine a trajectory between penumbra terminator points which satisfies Equation (33). This dilemma can be circumvented by introducing a virtual control variable, $\check{u}$, on the estimation of the time derivative t' during the eclipsed orbit phase. In this manner, the dynamic constraints become

$$\mathbf{f}(\mathbf{x}, \check{u}, L) - [\, p'\ f'\ g'\ \hbar'\ k'\ \check{u}\,]^{\top} = \mathbf{0}. \tag{38}$$

Now, to ensure that Equation (38) accurately approximates Equation (14), the following path constraint is introduced

$$\check{u} - \frac{\mathrm{d}t}{\mathrm{d}L} = 0. \tag{39}$$

As it is known that both time and true longitude increase monotonically throughout the orbit, an additional path constraint can be imposed on the control approximation such that

$$\check{u} > 0. \tag{40}$$

FIGURE 5 Comparison of the satellite state evolution while approximating $\frac{dt}{dL}$ using LGR collocation vs Keplerian dynamics for an example geostationary satellite transiting across an eclipse phase. LGR, Legendre-Gauss-Radau
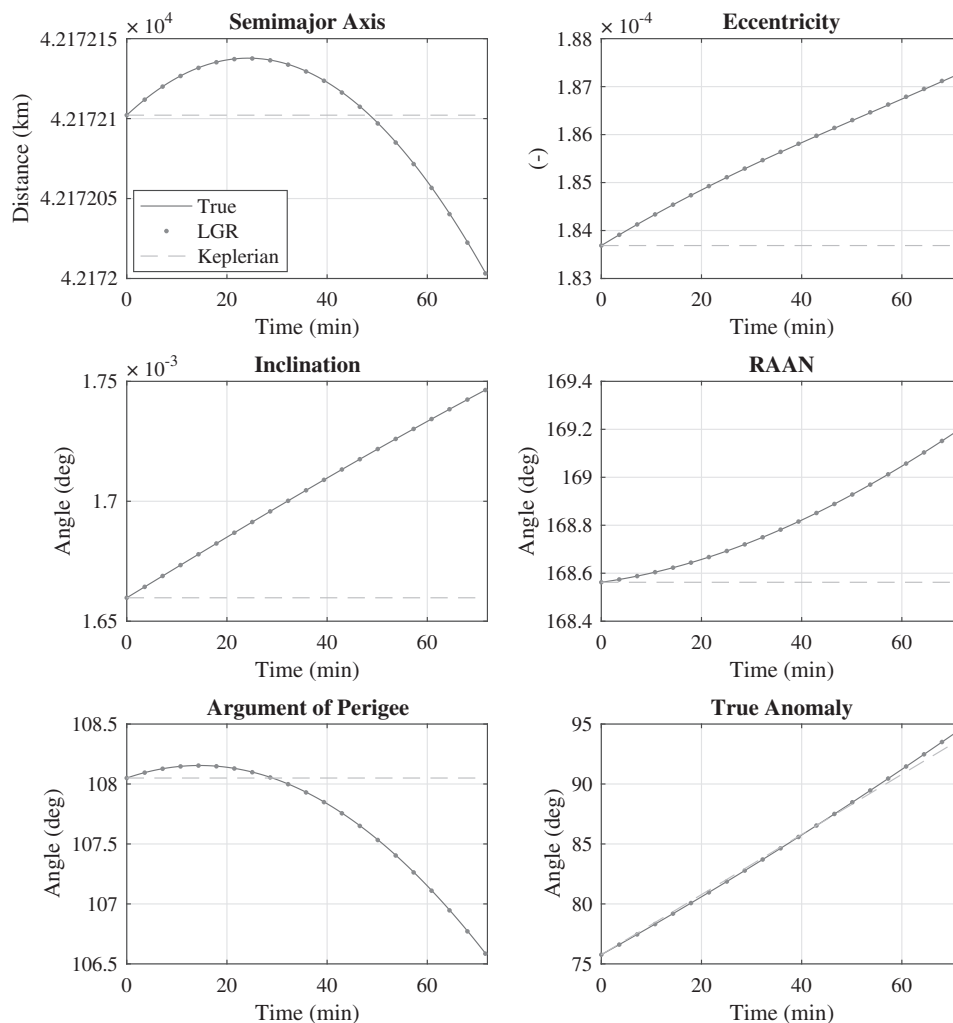
The NLP solver can now be tasked with accurately approximating the change in time with respect to true longitude as t' is a function of $\mathbf{x}$ and can be calculated at each LGR collocation point. This method approximates the state evolution exactly as a response to the gravitational perturbations. The differences in modeling using Keplerian vs LGR approximation can be seen in Figure 5 which illustrates the state evolution of an example geostationary spacecraft across an eclipsed phase of its orbit. From these results, the differences in approximation techniques is quite apparent. The semimajor axis values differ by approximately 100 m while the eccentricity and inclination differences continue to diverge. Significant differences are also captured in the ascending-node, perigee, and true anomaly angles, resulting in a cumulative true longitude difference of approximately 2°. When the accuracy of a solution is of high concern, these discrepancies can accumulate into misleading performance characteristics. For example, the trajectories produced in this work can be characterized by approximately 20 passes through eclipse regions, providing ample opportunity for compounded Keplerian approximation inaccuracies. Ultimately the LGR collocation scheme more accurately tracks the true dynamics when compared with the Keplerian propagation technique, leading to an improved representation of the spacecraft motion.

4.2.2 | Eclipsed solution algorithm

Equipped with a method to accurately approximate the spacecraft dynamics along an eclipse phase, a procedure to obtain minimum time maneuvering solutions with eclipsing is now introduced. As with the non-eclipsing problem, the eclipsed solution will be structured based on the initial guess on L_f and t_f. Furthermore, instead of determining estimates of L_f and t_f across a single mesh, terminator points must be accurately approximated for P phases

of the multiphase eclipsing problem. Specifically, estimates of $[L_0^{(i)}, L_f^{(i)}]$ and $[t_0^{(i)}, t_f^{(i)}]$ must be made for each phase $i \in \{1, 2, \dots, P\}$. Fortunately, these values can be readily obtained by postprocessing the non-eclipsing solutions and determining values of L and t which satisfy $\theta_r = \theta_p$ from Equation (33). For each phase, an initial guess of $\mathbf{x}$ and $\mathbf{u}$ is provided only at the terminator points $L_0^{(i)}$ and $L_f^{(i)}$ in a similar fashion as with the non-eclipsing case, so as not to over-bias the solution. Recall, as estimates for t are known from postprocessing, only $\{p, f, g, \hbar, k\}$ remain to be defined in $\mathbf{x}$ at the terminator points. Finally, the mesh intervals must be initialized for each of the P phases.

For the eclipsing results in this study, all trajectories are characterized by a single, fully illuminated, multirevolution trajectory immediately preceded or followed by a number of alternating eclipsed and illuminated phases. This is a consequence of the selection of Julian Dates for the simulated scenarios. As a result, $P - 1$ phases are initialized with a mesh consisting of a single mesh interval with four collocation points for cubic approximations of the spacecraft trajectory. The remaining phase is addressed similarly as the non-eclipse case, where the mesh is divided into N intervals corresponding to the number of completed revolutions within the multirevolution phase. For cases where trajectories are initialized near eclipse dates, denoted *Case A*, phase $i = P$ will be the multirevolution phase. Conversely, trajectories which terminate near eclipse dates, denoted *Case B*, phase $i = 1$ will be the multirevolution phase.

To obtain minimum time eclipsing solutions, revolutions may be added or subtracted from the initial guess derived from the non-eclipse solution, which requires additional consideration due to the existence multiple phases. When modifying revolutions for Case A, the procedure is similar to that of the non-eclipsing case, where N is updated in phase P, and the initial guess for $L_f^{(P)}$ and $t_f^{(P)}$ is updated. For Case B, N remains fixed in the multirevolution phase, and the number of phases must be altered instead. All additional revolutions are accompanied by the addition of two phases: one eclipsed phase and one illuminated phase. As a result, revolutions may be added such that phase $i = P + 1$ is defined using

$$\mathbf{x}_0^{(P+1)} = \mathbf{x}_f^{(P)} \quad \mathbf{x}_f^{(P+1)} = \mathbf{x}_f^{(P)}, \tag{41a}$$

$$\mathbf{u}_0^{(P+1)} = \mathbf{u}_f^{(P)} \quad \mathbf{u}_f^{(P+1)} = \mathbf{u}_f^{(P)}, \tag{41b}$$

$$L_0^{(P+1)} = L_f^{(P)} \quad L_f^{(P+1)} = L_f^{(P)} + \frac{\pi}{2}, \tag{41c}$$

$$t_0^{(P+1)} = t_f^{(P)} \quad t_f^{(P+1)} = t_f^{(P)} + 0.25 \text{ days}, \tag{41d}$$

and phase $i = P + 2$ is defined through

$$\mathbf{x}_0^{(P+2)} = \mathbf{x}_f^{(P+1)} \quad \mathbf{x}_f^{(P+2)} = \mathbf{x}_f^{(P+1)}, \tag{42a}$$

$$\mathbf{u}_0^{(P+2)} = \mathbf{u}_f^{(P+1)} \quad \mathbf{u}_f^{(P+2)} = \mathbf{u}_f^{(P+1)}, \tag{42b}$$

$$L_0^{(P+2)} = L_f^{(P-1)} \quad L_f^{(P+2)} = L_f^{(P)} + 2\pi, \tag{42c}$$

$$t_0^{(P+2)} = t_f^{(P-1)} \quad t_f^{(P+2)} = t_f^{(P)} + 1 \text{ day}, \tag{42d}$$

where, once again, the state definitions in Equations (41a) and (42a) refer to variables $\{p, f, g, \hbar, k\}$ as t is defined as in Equations (41d) and (42d). If it is determined that phases should be removed while searching for the minimum time eclipsing solution, the final phases can simply be removed from the problem transcription, starting with phase $i = P$ and working backwards towards phase $i = 1$ as necessary. The procedure for obtaining the minimum time solution is detailed in Algorithm 2.

Algorithm 2. Minimum time solution procedure with eclipsing

---

1. **Initialization**
   - i Obtain non-eclipsed solution
   - ii Postprocess non-eclipsed solution to obtain $[L_0^{(i)}, \sim L_f^{(i)}]$ and $[t_0^{(i)}, \sim t_f^{(i)}]$ $\forall i \sim\in \{1, \sim 2, \sim \ldots, \sim P\}$
   - iii Supply initial guess for **x** and **u** at each $[L_0^{(i)}, \sim L_f^{(i)}]$ pairing
   - iv Determine N associated with phase P
   - v Define solution counter $i_{sol} = 0$

2. **Optimization**
   - i Divide mesh interval on phase P into N equally spaced intervals
   - ii Define a single mesh interval to each of the remaining $P - 1$ phases
   - iii Attempt minimum time solution using GPOPS-II with SNOPT

3. **Termination Tests**

Case A:

  if solution is found **then**

    i Set $i_{sol} = i_{sol} + 1$
    ii Set $t_f^{\star} = t_f^{(P)}$
    iii Set $N = N - 1$
    iv Go back to step 2
  else if $i_{sol} > 1$ **then**

    i Set $N = N + 1$
    ii Go back to step 2
  else

    i Terminate search algorithm
    ii $t_f^{\star}$ is minimum time solution
  end if

Case B:

  if solution is found **then**

    i Set $i_{sol} = i_{sol} + 1$
    ii Set $t_f^{\star} = t_f^P$
    iii Remove phase P from trajectory
    iv Set $P = P - 1$
    v Go back to step 2
  else if $i_{sol} > 1$ **then**

    i Add phase $P + 1$ in accordance with Equation (41)
    ii Add phase $P + 2$ in accordance with Equation (42)
    iii Set $P = P + 2$
    iv Go back to step 2
  else

    i Terminate search algorithm
    ii $t_f^{\star}$ is minimum time solution
  end if

Specific definitions on bounds and initial guess definitions are provided in the following section.

5 | NUMERICAL RESULTS

Equipped with a strategy to generate minimum time solar sail trajectories for both eclipsed and non-eclipsed maneuvering, solutions to the deorbit and rephasing problems can now be obtained. Recall, NLP solver SNOPT is used in this work with adaptive mesh refinement executed using GPOPS-II. Mesh intervals have been allowed up to eight collocation points before being subdivided, with mesh refinement tolerance set to 10^{-6} and overall SNOPT tolerance set to 10^{-6}. For the simulations to follow, a 100 kg sail-craft with 1200 m^2 sail area is simulated to either deorbit a 1100 kg payload or rendezvous with a desired slot in the GEO belt; as a result, the deorbit maneuvers result in a 1 $\frac{m^2}{kg}$ area to mass system while the rendezvous maneuvers result in a 12 $\frac{m^2}{kg}$ area to mass system. The following results help to characterize the current capabilities of solar sails for high-altitude orbital debris mitigation.

5.1 | Deorbit solutions

To address the minimum time deorbit maneuver, a solution to the following optimal control problem is desired

$$\underset{\theta(t)}{\arg\min} \quad t_f, \tag{43a}$$

s.t.

$$\ddot{\mathbf{r}} - \frac{\mu_\oplus}{r^3}\mathbf{r} = \mathbf{a}_d, \tag{43b}$$

$$[\, a_0 \; e_0 \; i_0 \,]^\mathsf{T} = [\, r_{\text{GEO}} \; 0 \; 0 \,]^\mathsf{T}, \tag{43c}$$

$$e_f \leq 0.003, \tag{43d}$$

$$r_{p,f} \geq r_{\text{GEO}} + 250 \text{ km}, \tag{43e}$$

$$0 \leq \theta(t) \leq \frac{\pi}{2}, \tag{43f}$$

where the cost function $J = t_f$ is to be reduced using the sun-sail angle $\theta(t)$ from Equation (11). Equality constraints 43b and 43c provide the dynamic constraints and initial conditions for a geostationary satellite orbit, respectively. Inequality constraints 43d and 43e are event constraints which define satisfactory deorbit of the debris fragment into the graveyard orbit. The value $r_{\text{GEO}} + 250$ km comes as a result of Table B2 for the $1 \frac{\text{m}^2}{\text{kg}}$ system simulated here. The final inequality in Equation (43f) serves as a path constraint on the sail orientation, restricting sail solutions to produce orientations which point the sail surface normal towards the sun. For this optimization problem, the state is resolved in the MEOE set. Practical limitations can be placed based on expected orbital behaviors from Reference 31, resulting in

$$
\begin{aligned}
r_{\text{GEO}} \leq p \leq r_{\text{GEO}} + 1000 \text{ km} \qquad & -0.1 \leq \hbar \leq 0.1 \\
-0.01 \leq f \leq 0.01 \qquad & -0.1 \leq k \leq 0.1 \\
-0.01 \leq g \leq 0.01 \qquad & 0 \leq t \leq N \text{ days}
\end{aligned}
\tag{44}
$$

Limitations on the true longitude are defined as

$$L_0 \leq L \leq N \text{ revs}, \tag{45}$$

where $L_0 = 0$, nominally. For the sake of initializing all simulations in direct sunlight, the autumnal simulations begin with an initial true longitude of $L_0 = \pi$, as $L_0 = 0$ initializations place the spacecraft in eclipse.

The boundary condition from Equation (43c) specifies the ideal orbital definitions for a geostationary satellite. The resulting initial conditions in the MEOE set are

$$
\begin{aligned}
\mathbf{x}_0 &= [\, p_0 \; f_0 \; g_0 \; \hbar_0 \; k_0 \; t_0 \,]^\mathsf{T} \\
&= [\, r_{\text{GEO}} \; 0 \; 0 \; 0 \; 0 \; 0 \,]^\mathsf{T}
\end{aligned}
\tag{46}
$$

Terminal conditions must satisfy Equations (43d) and (43e), placing restrictions directly on COE variables a and e and MEOE variables p, f, and g. To determine bounds on the acceptable terminal state values, Equation (43e) provides

$$p_f \geq (1 + e_f)(r_{\text{GEO}} + 250 \text{ km}) \tag{47}$$

based on $r_p \triangleq \frac{p}{1+e}$, the radius of perigee expressed in terms of the semiparameter and eccentricity. From Equation (43d), the minimum eccentricity of $e = 0$ provides the lower bound on p_f, resulting in

$$r_{\text{GEO}} + 250 \text{ km} \leq p_f. \tag{48}$$

Furthermore, the eccentricity bounds result in the following limits on f_f and g_f

$$-0.003 \leq \{f_f, \; g_f\} \leq 0.003. \tag{49}$$

Elements $\hbar$, k, and t, as well as L are free parameters, with no additional constraints on the initial or terminal conditions. Ultimately, the estimate of the final state $\tilde{\mathbf{x}}_f = [\ \tilde{p}_f\ \tilde{f}_f\ \tilde{g}_f\ \tilde{h}_f\ \tilde{k}_f\ \tilde{t}_f\ ]^{\mathsf{T}}$ is selected such that

$$
\begin{aligned}
\tilde{p}_f &= 1.003 \cdot (r_{\text{GEO}} + 250 \text{ km}) & \tilde{h}_f &= 0.1 \\
\tilde{f}_f &= 0.003 & \tilde{k}_f &= 0 \\
\tilde{g}_f &= 0 & \tilde{t}_f &= 50 \text{ days}
\end{aligned}
\tag{50}
$$

where N is chosen to be 50, resulting in $\tilde{L}_f = 50$ revs. These conditions define a candidate solution where $r_{p,f} = r_{\text{GEO}} + 250$ km and $e = 0.003$. The selection of $N = 50$ was made to deliberately underestimate the duration of the deorbit maneuvers and allow the search algorithms detailed in Section 4 to perform across a broad solution space.

Recall from Section 3 that a locally optimal sail orientation exists with respect to some prescribed constraint or primer vector $\boldsymbol{\zeta}$ whose orientation defines the response of the closed form, locally optimal solution. As the sail orientation seeks to manipulate some combination of e and r_p in minimal time, the primer vector can be reasonably restricted to the $\hat{\mathbf{r}}$-$\hat{\mathbf{s}}$ plane ($u_w = 0$). This further reduces the dimensionality of the unknown control variables, resulting in the updated path constraint

$$
u_r^2 + u_s^2 = 1
\tag{51}
$$

with individual control components restricted to

$$
-1 \leq \{u_r,\ u_s\} \leq 1.
\tag{52}
$$

In this manner, the control can be reduced to a single vector component as $u_r = \sqrt{1 - u_s^2}$. It is noted, however, that for the results that follow, individual components $\{u_r,\ u_s\}$ are approximated separately while satisfying Equation (51), as this method generated more convergence capability in practice. Regardless of the selection of $\tilde{\boldsymbol{\zeta}}$ from $\mathbf{u}$, Equation (43f) will be satisfied automatically from the resulting $\{\ \alpha^\star,\ \beta^\star\ \}$ combination as defined in the optimization basis in Figure 2. Here, control estimates at L_0 and L_f were arbitrarily defined to be

$$
\tilde{\mathbf{u}}_0 = [\ 1\ 0\ ]^{\mathsf{T}}
\tag{53}
$$

and

$$
\tilde{\mathbf{u}}_f = [\ 0\ 1\ ]^{\mathsf{T}}
\tag{54}
$$

respectively.

To illustrate the feasibility of minimum time solar sailing deorbit, solutions to Equation (43) are sought for four test scenarios. The dates for the test cases are selected so as to coincide with the solstices and equinoxes of year 2018. The results of the non-eclipsed maneuvers are presented first which serve as initial guesses for the eclipsed maneuvering solutions. Table 1 summarizes the optimized, non-eclipsed deorbit maneuver.

From these obtained solutions, eclipse terminator points are obtained via postprocessing and an initial mesh is formed based on the anticipated solution structure. Bounds on all $L_f^{(i)}$ and intermediate $L_0^{(i)}$ variables were set to $\pm 2\pi$ of their guessed values, with bounds on the associated $t_f^{(i)}$ and intermediate $t_0^{(i)}$ times set to ± 1 day of the supplied guess values.

TABLE 1 Minimum time deorbit results for 1.00 $\frac{\text{m}^2}{\text{kg}}$ system based on initial date

Initial date	Total time (days)	Total revolutions
Vernal equinox	89.1230	88.7810
Summer solstice	92.4514	92.1154
Autumnal equinox	88.8666	89.0322
Winter solstice	86.6965	86.3645
Average	89.2844	89.0755

Event constraints are defined at the junctions of each phase using

$$\mathbf{x}_0^{(i+1)} - \mathbf{x}_f^{(i)} = \mathbf{0}, \tag{55a}$$

$$L_0^{(i+1)} - L_f^{(i)} = 0, \tag{55b}$$

to be enforced for all $i \in \{ 1, 2, \ldots, P - 1 \}$. To ensure each intermediate phase is bounded by an eclipsing event, additional event constraints from Equation (33) are imposed at the boundaries as

$$\theta_r^{(i)} - \theta_p^{(i)} = 0. \tag{56}$$

During an eclipse phase, the path constraint

$$\theta_r^{(i)} - \theta_p^{(i)} \leq 0 \tag{57}$$

must be satisfied while illuminated phases must satisfy

$$\theta_p^{(i)} - \theta_r^{(i)} \leq 0 \tag{58}$$

along the trajectory.

Results from the eclipsed maneuvering cases are compiled in Table 2 with state and control parameters provided in Figures 6 to 8 for the winter case. The best sail performance occurs near the winter solstice, with vernal and autumnal equinox solutions exhibiting similar performance characteristics, and the summer solstice solution requiring the most time for deorbit. The coupling between perigee and eccentricity behaviors is shown in Figure 6. During the first 40 days of maneuvering, the eccentricity demonstrates a drastic rise to the retirement threshold value while the perigee increases with small acceleration. Beyond this first 40 days, the secular trends in eccentricity and perigee remain mostly constant with eccentricity steady about 0.003 and perigee linearly increasing to the threshold value. Analysis of the solution structure for all deorbit control approximations indicates a primer vector profile which evolves according to a repeated, tangent behavior as shown in Figure 7, where discontinuities in the control are apparent as a result of eclipsing.

Consistent among all simulations is the presence of eclipse regions. Eclipse regions occur at the ends of the summer and winter initialized simulations, when the Earth is beginning to enter the equinoctial regions. Alternatively, simulations initialized on the vernal and autumnal equinoxes begin their maneuvers in the middle the Earth's eclipse seasons. Observing the state evolution in Figure 8, a noticeable eclipsing impact exists, highlighting the sensitivity of the state dynamics to the control, particularly in the semimajor axis and argument of perigee plots. Compared with the non-eclipsed solutions, the minimum time deorbit solutions are characterized by nearly one additional day of maneuvering accompanied by nearly one additional revolution about the Earth. These results appear to be attributed directly to the lack of SRP control while in eclipse, as the average time spent in shadow amounts to 21.03 hours for a deorbit maneuver.

TABLE 2 Results of minimum time deorbit maneuver with eclipsing for the 1 $\frac{m^2}{kg}$ satellite system initialized at the start of each season

Initial date	Total time (days)	Total revolutions	Eclipse time (hours)	Phase count
Vernal equinox	90.07	89.75	21.66	47
Summer solstice	93.30	92.93	21.20	45
Autumnal equinox	89.10	89.30	21.47	45
Winter solstice	87.83	87.47	19.79	44
Average	90.00	89.86	21.03	∼ 45

FIGURE 6 Perigee and eccentricity histories for minimum time deorbit with eclipsing from 2018 winter solstice
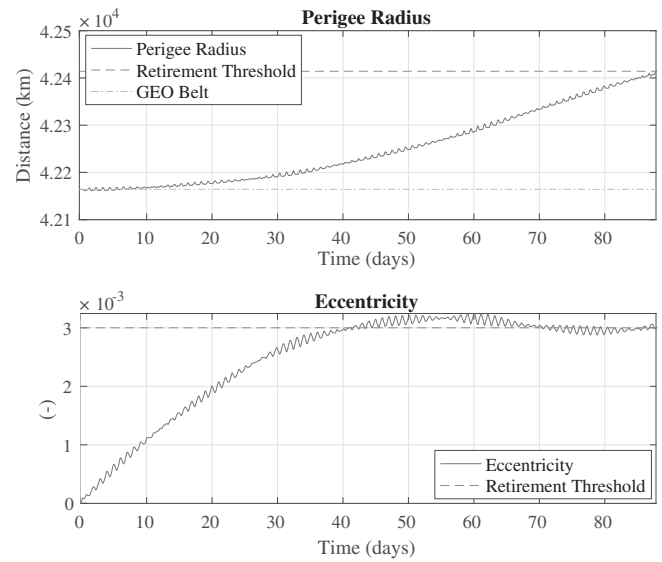
FIGURE 7 Zoomed optimal control solution for minimum time deorbit with eclipsing from 2018 winter solstice. Control discontinuities due to eclipsing deorbit
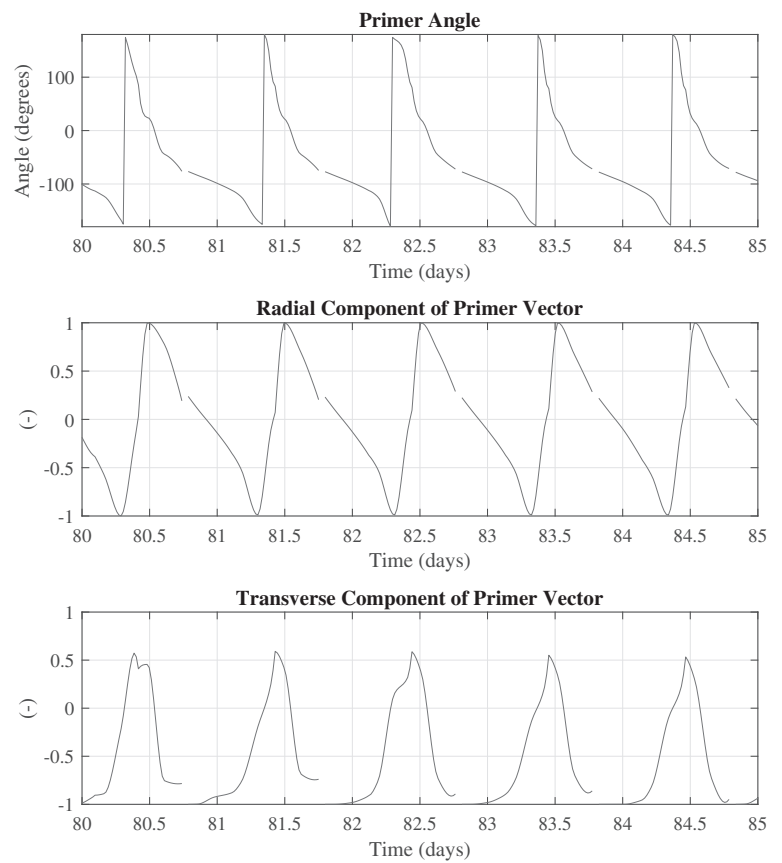
5.2 | Phasing solutions

To obtain a minimum time phasing solution, the maneuver is transcribed into the following optimal control problem

$$\underset{\theta(t)}{\arg\min} \quad t_f, \tag{59a}$$

s.t.

$$\ddot{\mathbf{r}} - \frac{\mu_\oplus}{r^3}\mathbf{r} = \mathbf{a}_d, \tag{59b}$$

$$[\, a_0 \; e_0 \; i_0 \,] = [\, (r_{\mathrm{GEO}} + 250 \text{ km})\; 0 \; 0 \,], \tag{59c}$$

$$a_f = r_{\mathrm{GEO}}, \tag{59d}$$

$$e_f \leq \frac{200 \text{ km}}{r_{\mathrm{GEO}}}, \tag{59e}$$

$$i_f \leq 15°, \tag{59f}$$

$$|\phi_f| \leq 1°, \tag{59g}$$

$$0 \leq \theta(t) \leq \frac{\pi}{2}. \tag{59h}$$

This optimal control problem seeks a minimum time solution which transfers a sail-craft from an arbitrary graveyard orbit to a desired slot within the GEO belt. In an *ECEF* coordinate system, the spacecraft has longitude λ and the location of the desired GEO slot has longitude λ_{GEO}. Using these angles, the phase error ϕ is introduced as

$$\phi = \mathrm{mod}(\lambda - \lambda_{\mathrm{GEO}},\; 2\pi) - \pi, \tag{60}$$

where mod() is the modulo operator and the subtraction of π is used in calculations to bound $\phi \in [-\pi,\; \pi]$. This phase error will be used here to determine the relative longitude between the sail-craft and the desired GEO belt location.
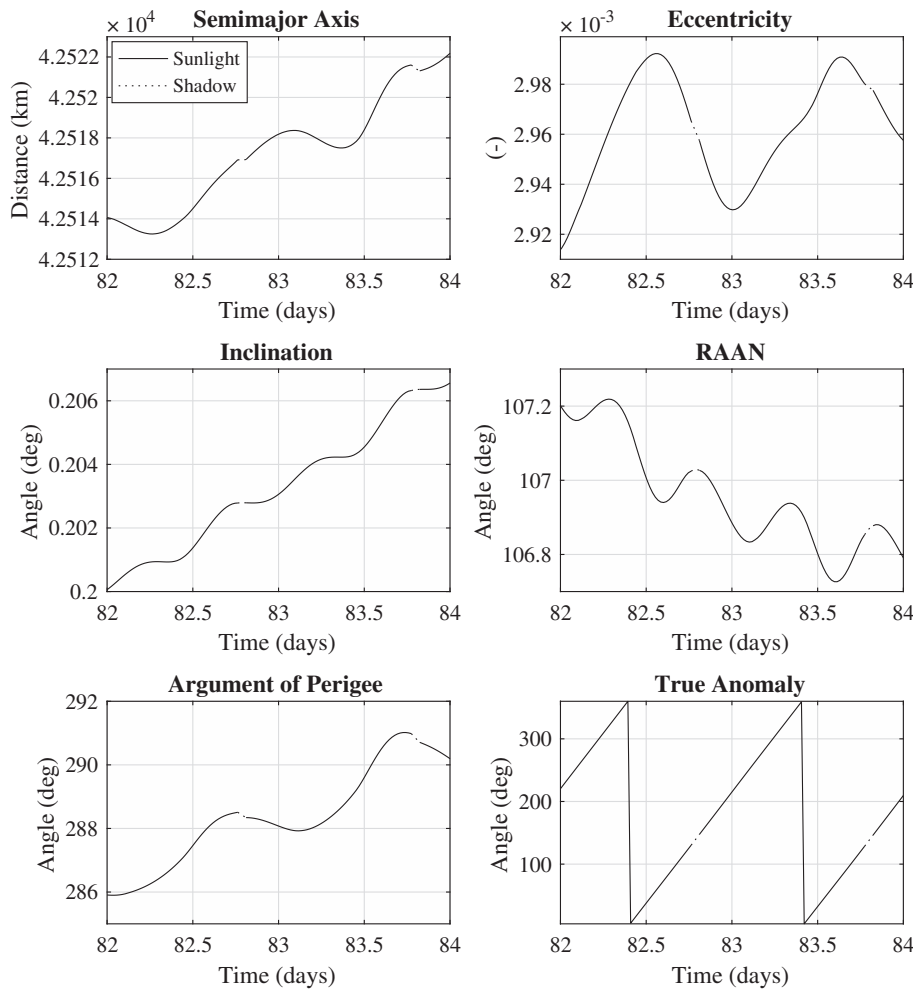
FIGURE 8 Classical orbital element evolution as a result of eclipsing considerations for 2018 winter solstice deorbit

TABLE 3 Results of minimum time GEO slot rendezvous maneuver for January 1, 2018 start date

Initial ϕ	Total time (days)	Number of revolutions	Eclipse time (hours)	Number of phases
0°	8.08	8.10	0	1
90°	60.44	61.35	2.45	11
180°	50.79	51.43	0	1
270°	38.02	38.37	0	1

Abbreviation: GEO, geostationary orbits.

From Equation (59), dynamic constraints are included through Equation (59b) and are identical to Equation (43b). Equality constraint 59c initializes the satellite orbit with minimum satisfactory deorbit conditions as defined by the IADC. Constraints contained in Equations (59d) to (59f) define terminal conditions which must be satisfied simultaneously to ensure placement of the spacecraft within the protected GEO region as defined by the IADC. With a geosynchronous semimajor axis, the period of the final orbit is known to at least be equal to one sidereal day. The eccentricity constraint on the final orbit ensures that the spacecraft is no more than 200 km from the GEO belt. Equation (59g) constrains the final phase error, ϕ_f, to be less than one degree. Finally, Equation (59h) serves as an inequality constraint which ensures the SRP force contributions act in a direction opposing the sun direction vector ($\hat{\boldsymbol{e}}_\odot$).

Four time-optimal GEO slot rendezvous scenarios are now addressed, initialized on January 1, 2018, from a perfectly circular disposal orbit of radius $r_0 = r_{GEO} + 250$ km with initial phase errors of $\phi_0 = \{0°,\ 90°,\ 180°,\ 270°\}$. These initial phase error selections will prove the rendezvous capabilities of a solar sailing spacecraft regardless of the desired final longitude about the Earth. Recall, the area to mass ratio is calculated assuming a 1200 m² sail-craft of 100 kg mass, resulting in a 12 $\frac{m^2}{kg}$ system without payload.

For the minimum time rendezvous problem, the iterative search method is employed using $N = 5$ to, once again, deliberately underestimate the duration of the true minimum time solution. As with the deorbit maneuvers, limitations on the state were defined as indicated in Equation (44). The initial state for the rendezvous maneuver is defined as

$$\mathbf{x}_0 = [\ p_0\ f_0\ g_0\ \hbar_0\ k_0\ t_0\ ]^\mathsf{T}$$
$$= [\ (r_{GEO} + 250\ \text{km})\ 0\ 0\ 0\ 0\ 0\ ]^\mathsf{T} \tag{61}$$

with a guess supplied on the final state such that

$$\tilde{p}_f = r_{GEO} - \frac{(200\ \text{km})^2}{r_{GEO}} \qquad \tilde{\hbar} = 0$$
$$\tilde{f} = \frac{200\ \text{km}}{r_{GEO}} \qquad \hat{k} = 0$$
$$\tilde{g} = 0 \qquad \tilde{t}_f = N\ \text{days} \tag{62}$$

This guess places the spacecraft just within the GEO region with zero inclination at some final time $\tilde{t}_f$ based on the IADC definitions in Table B1. To restrict solutions to regions about the GEO belt, bounds on the state are set to

$$r_{GEO} - 1000\ \text{km} \le p \le r_{GEO} + 1000\ \text{km} \qquad -0.1 \le \hbar \le 0.1$$
$$-0.05 \le f \le 0.05 \qquad -0.1 \le k \le 0.1$$
$$-0.05 \le g \le 0.05 \qquad 0 \le t \le t_{max} \tag{63}$$

with true longitude bounds of integration $L \in [0,\ N\ \text{revs}]$ for all four rendezvous cases. The control is structured similarly as with the minimum time deorbit simulations, where control guesses are supplied at the terminator points of each potential phase using Equations (53) and (54). As control solutions are again restricted to the $\hat{r}$-$\hat{s}$ plane, control bounds are defined through Equation (52) while adhering to unity constraint Equation (51).

Results from the phasing scenarios are compiled in Table 3. The 90° initial phase error simulation is selected to illustrate the orbit profile associated with the phasing maneuvers as displayed in Figures 9 and 10.
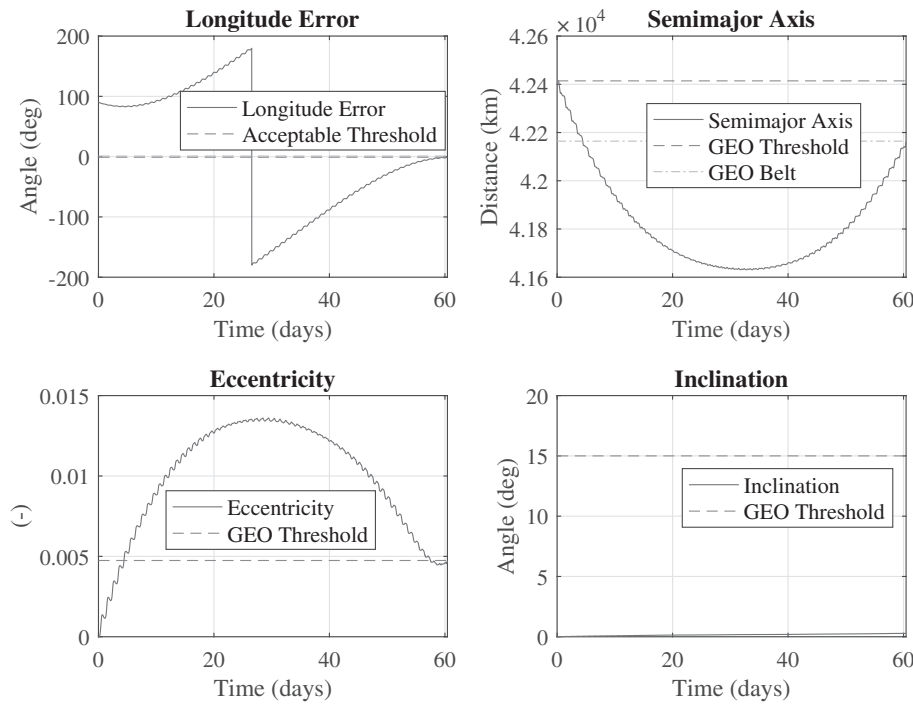
FIGURE 9 Satellite trajectory for minimum time GEO rendezvous maneuver with longitude error, semimajor axis, eccentricity profiles, and inclination. Initial longitude error is 90°. GEO, geostationary orbits
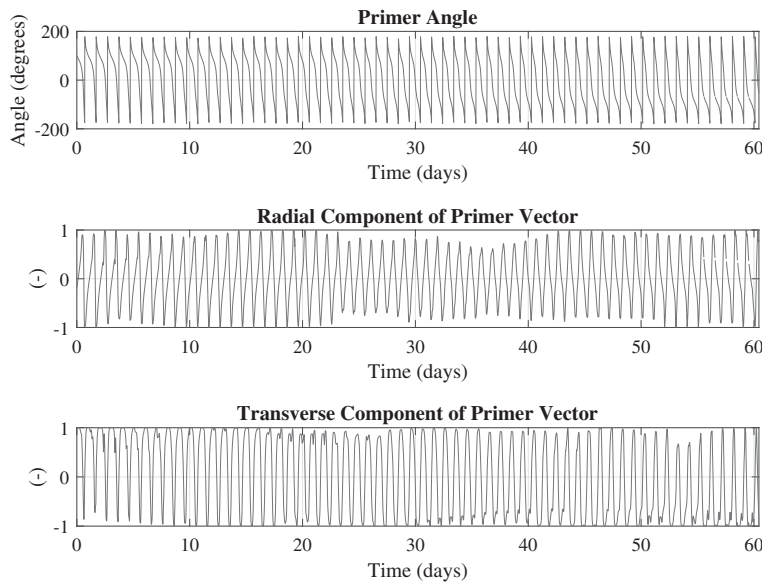
FIGURE 10 Optimal control solution for minimum time GEO rendezvous maneuver with 90° initial longitude error. GEO, geostationary orbits

Figure 9 provides a rendezvous profile where the sail-craft lowers its semimajor axis below the GEO belt in order to reduce the phasing difference between its current and desired longitudes then subsequently increases the semimajor axis to the geosynchronous value once the sail-craft is appropriately phased. Here, rendezvous solutions are obtained in a matter of months, as opposed to years as suggested in Reference 31. The longitude error, semimajor axis, and eccentricity profiles exhibit nearly symmetric behaviors and are more quickly brought to within their desired thresholds as a result of the significant increase in area to mass ratio compared with the deorbit scenarios. The inclination, however, appears largely unaffected by the sail maneuvers, and varies slowly as a result of gravitational disturbances. From Reference 31, it is known that the dynamics associated with changes in semimajor axis, eccentricity, and phase error are attributed to applied forces in the $\hat{r}$-$\hat{s}$ plane while inclination variations are dependent upon $\hat{w}$ contributions. This phenomenon is made apparent here as the inclination behavior in Figure 9 shows very little response to sail inputs which have contributions only in the $\hat{r}$-$\hat{s}$ plane by design. As the TugSat concept is not expected to operate beyond the 15° limit defined by the IADC, inclination ranges for the intended use-cases will have minimal impact on the phasing control solution.

Similar to the deorbit maneuvers, the primer vector control solution in Figure 10 displays repeating tangent-like behavior, periodic with each completed revolution. By examination of the full control profile, the specific structure of the control approximation is observed to trend such that control solutions at the beginning and end of the maneuver appear inverted from one another. Physically, this is attributed to the sail first maneuvering to lower the spacecraft orbit, while reducing the phase error, then subsequently increasing the spacecraft orbit to remain in the correct longitude at a geosynchronous altitude.

For all test cases analyzed here, the optimal phasing method is implemented as an orbit lowering method in order to catch up to the GEO slot of interest. Physically, the angular velocity of the spacecraft increases and the orbital period decreases, resulting in a decrease in the phase error. Raising the orbit by a similar increment in altitude would not amount to the same capability in phase error reduction as the mean motion of a spacecraft changes with respect to semimajor axis by a factor of $a^{-\frac{3}{2}}$. In addition, the rendezvous time required for the 0° phase error simulation is significantly shorter as the penalty incurred by the spacecraft's change in semimajor axis was not enough to bring the eccentricity above the threshold defined by the IADC. For the { 90°, 180°, 270° } simulations which did exceed the IADC threshold during maneuvering, the final rendezvous time seem to differ by approximately 10 days per 90° of initial phase error.

6 | CONCLUSION

SRP is a feasible means of propulsion for applications near the GEO belt such as high-altitude orbital debris mitigation. The orbit transfer problem serves as proof of concept that SRP is a meaningful propulsion source, with suggested use with small satellites. The planar rephasing problem further validates SRP propulsion as a means of more precise orbital maneuvering, allowing for sufficient terminal proximity to some desirable orbit before more traditional relative motion dynamic and control strategies can be implemented. Furthermore, the resulting solution structure presents a novel blend of underactuated, low-thrust control using quadrature techniques with abundant nonlinear path and event constraints. The solutions to these problems may translate to cost-effective propulsion solutions for long-term, propellantless science missions.

The TugSat mission concept is used to validate the effectiveness of the SRP propulsion methods through deorbit and longitude targeting simulations designed to represent potential debris mitigation techniques in the GEO belt. Ultimately, the TugSat maneuvers provide deorbit and subsequent rendezvous capability for durations on the order of months as opposed to years as suggested in previous works. Notably, an entire deorbit and GEO belt rendezvous maneuver can be accomplished using numerical optimization methods in less time than it would take for a single deorbit maneuver in either Kelly et al[31] or Kelly and Bevilacqua.[32]

Finally, the optimized primer vector and improved eclipse handling techniques introduced here are not restricted to the solar sailing problem. Optimized primer vector orientations can be sought for any CLT orbit transfer problem, offering an alternative means of trajectory design or initial guess generation. In addition, large time-scale, multirevolution maneuvers subject to eclipsing can be addressed with more realistic state approximations, thus producing more accurate minimum time solutions.

ORCID

Patrick Kelly https://orcid.org/0000-0002-9128-631X

REFERENCES

1. Früh C, Schildknecht T. Variation of the area-to-mass ratio of high area-to-mass ratio space debris objects. *Monthly Notices Royal Astronom Soc*. 2012;419(4):3521-3528. https://doi.org/10.1111/j.1365-2966.2011.19990.x.
2. Betts JT, Erb SO. Optimal low thrust trajectories to the moon. *SIAM J Appl Dyn Syst*. 2003;2(2):144-170.
3. Betts JT. Optimal low-thrust orbit transfers with eclipsing. *Opt Control Appl Methods*. 2015;36(2):218-240. https://doi.org/10.1002/oca.2111.
4. Graham KF, Rao AV. Minimum-time trajectory optimization of multiple revolution low-thrust earth-orbit transfers. *J Spacecraft Rockets*. 2015;52(3):711–727. https://arc.aiaa.org/doi/full/10.2514/1.A33187.
5. Graham KF, Rao AV. Minimum-time trajectory optimization of low-thrust earth-orbit transfers with eclipsing. *J Spacecraft Rockets*. 2016;53(2):289-303. https://doi.org/10.2514/1.A33416.
6. Ross IM, Gong Q, Sekhavat P. Low-thrust, high-accuracy trajectory optimization. *J Guid, Control Dyn*. 2007;30(4):921-933. https://doi.org/10.2514/1.23181.

7. Tsuda Y, Mori O, Funase R, et al. Achievement of IKAROS - Japanese deep space solar sail demonstration mission. *Acta Astronautica*. 2013;82(2):183-188. https://doi.org/10.1016/j.actaastro.2012.03.032.

8. Ridenoure RW, Munakata R, Wong SD, et al. Testing the lightsail program: advancing solar sailing technology using a cubesat platform. *J Small Satellites*. 2016;5(2):531-550.

9. McNutt L, Johnson L, Kahn P, Castillo-Rogez J, Frick A. Near-earth asteroid (NEA) scout. *AIAA SPACE Forum*. San Diego, CA; 2014;4435. https://doi.org/10.2514/6.2014-4435.

10. Heiligers J, Diedrich B, Derbes W, McInnes C. Sunjammer: preliminary end-to-end mission design. Paper presented at: Proceedings of the AIAA/AAS Astrodynamics Specialist Conference. San Diego, CA; 2014:4127.

11. Steering Group and Working Group 4. *IADC Space Debris Mitigation Guidelines. Technical Report IADC-02-01, Revision 1*. Inter-Agency Space Debris Coordination Committee; 2007.

12. Steering Group and Working Group 4. *IADC Space Debris Mitigation Guidelines. Technical Report IADC-04-06, Revision 5.5*. Inter-Agency Space Debris Coordination Committee; 2014.

13. Jehn R, Agapov V, Hernández C. The situation in the geostationary ring. *Adv Space Res*. 2005;35(7):1318-1327. https://doi.org/10.1016/j.asr.2005.03.0222.

14. Allen J. The Galaxy 15 anomaly: another satellite in the wrong place at a critical time. *Space Weather*. 2010;8(6):S06008. https://doi.org/10.1029/2010SW000588.

15. Castet JF, Saleh JH. Satellite and satellite subsystems reliability: statistical data analysis and modeling. *Reliab Eng Syst Safety*. 2009;94(11):1718-1728. https://doi.org/10.1201/9780203859759.ch121.

16. Fekete TA. Trajectory Design for Solar Sailing from Low-Earth Orbit to the Moon [Master's thesis]. Massachusetts Institute of Technology; 1991.

17. Pagel G. Extremale Steuerstrategien für Sonnensegler am Beispiel von Bahntransferproblemen zum Erdmond [PhD thesis]. Technische Universität Berlin; 2002.

18. Howell KC, Wawrzyniak GG. Generating solar sail trajectories in the earth-moon system using augmented finite-difference methods. *Int J Aerosp Eng*. 2011;2011. https://doi.org/10.1155/2011/476197.

19. Wawrzyniak GG, Howell KC. Numerical techniques for generating and refining solar sail trajectories. *Adv Space Res*. 2011;48(11):1848-1857. https://doi.org/10.1016/j.asr.2011.04.012.

20. Dachwald B. Optimal solar sail trajectories for missions to the outer solar system. *J Guid Control Dyn*. 2005;28(6):1187-1193. https://doi.org/10.2514/1.13301.

21. Peloni A, Ceriotti M, Dachwald B. Solar-sail trajectory design for a multiple near-earth-asteroid rendezvous mission. *J Guid Control Dyn*. 2016;39(12):2712-2724. https://doi.org/10.2514/1.G000470.

22. Peloni A, Rao AV, Ceriotti M. Automated trajectory optimizer for solar sailing (ATOSS). *Aerosp Sci Technol*. 2018;72:465-475. https://doi.org/10.1016/j.ast.2017.11.025.

23. Green AJ. Optimal Escape Trajectory from a High Earth Orbit by Use of Solar Radiation Pressure [Master's thesis]. Massachusetts Institute of Technology; 1977.

24. Sackett LL. *Optimal Solar Sail Planetocentric Trajectories. Technical Report R-1113*. Cambridge, MA: The Charles Stark Draper Laboratory, Inc; 1977.

25. Coverstone VL, Prussing JE. Technique for escape from geosynchronous transfer orbit using a solar sail. *J Guid Control Dyn*. 2003;26(4):628-634. https://doi.org/10.2514/2.5091.

26. Macdonald M, McInnes C. Analytical control laws for planet-centered solar sailing. *J Guid Control Dyn*. 2005;28(5):1038-1048. https://doi.org/10.2514/1.11400.

27. Macdonald M, McInnes C. Realistic earth escape strategies for solar sailing. *J Guid Control Dyn*. 2005;28(2):315-323. https://doi.org/10.1016/j.buildenv.2006.10.027.

28. Macdonald M, McInnes CR. Solar sail science mission applications and advancement. *Adv Space Res*. 2011;48(11):1702-1716. https://doi.org/10.1016/j.asr.2011.03.018.

29. Heiligers J, Ceriotti M, McInnes CR, Biggs JD. Displaced geostationary orbit design using hybrid sail propulsion. *J Guid Control Dyn*. 2011;34(6):1852-1866. https://doi.org/10.2514/1.53807.

30. Quarta AA, Mengali G. Approximate solutions to circle-to-circle solar sail orbit transfer. *J Guid, Control Dyn*. 2013;36(6):1886-1890. https://doi.org/10.2514/1.60307.

31. Kelly PW, Bevilacqua R, Mazal L, Erwin RS. TugSat: removing space debris from geostationary orbits using solar sails. *J Spacecraft Rockets*. 2018;55(2):437-450. https://doi.org/10.2514/1.A33872.

32. Kelly P, Bevilacqua R. An optimized analytical solution for geostationary debris removal using solar sails. *Acta Astronautica*. 2019;162 72–86. https://doi.org/10.1016/j.actaastro.2019.05.055.

33. Patterson MA, Rao AV. GPOPS-II: a MATLAB software for solving multiple-phase optimal control problems using hp-adaptive Gaussian quadrature collocation methods and sparse nonlinear programming. *ACM Trans Math Softw*. 2014;41(1):1:1-1:37. https://doi.org/10.1145/2558904.

34. Darby CL, Hager WW, Rao AV. An hp-adaptive pseudospectral method for solving optimal control problems. *Opt Control Appl Methods*. 2010;32(4):476-502. https://doi.org/10.1002/oca.957.

35. Darby CL, Hager WW, Rao AV. Direct trajectory optimization using a variable low-order adaptive pseudospectral method. *J Spacecraft Rockets*. 2011;48(3):433-445. https://doi.org/10.2514/1.52136.

36. Liu F, Hager WW, Rao AV. Adaptive mesh refinement method for optimal control using nonsmoothness detection and mesh size reduction. *J Frankl Inst*. 2015;352(10):4081-4106. https://doi.org/10.1016/j.jfranklin.2015.05.028.

37. Patterson MA, Hager WW, Rao AV. A ph mesh refinement method for optimal control. *Opt Control Appl Methods*. 2014;36(4):398-421. https://doi.org/10.1002/oca.2114.

38. Patterson MA, Rao AV. Exploiting sparsity in direct collocation pseudospectral methods for solving optimal control problems. *J Spacecraft Rockets*. 2012;49(2):354-377. https://doi.org/10.2514/A32071.

39. Gill PE, Murray W, Saunders MA. SNOPT: an SQP algorithm for large-scale constrained optimization. *SIAM Rev*. 2005;47:99-131.

40. Gill PE, Murray W, Saunders MA, Wong E. *User's Guide for SNOPT 7.7: Software for Large-Scale Nonlinear Programming. Center for Computational Mathematics Report CCoM 18-1*. San Diego; La Jolla, CA: Department of Mathematics, University of California; 2018.

41. Lara M, Elipe A. Periodic orbits around geostationary positions. *Celestial Mech Dyn Astronomy*. 2002;82(3):285-299. https://doi.org/10.1023/A:1015046613477.

42. Vallado DA. *Fundamentals of Astrodynamics and Applications*. Vol 9. 4th ed. Hawthorne, CA: Microcosm Press; 2013:609-730.

43. Montenbruck O, Gill E. *Satellite Orbits: Models, Methods and Applications*. Vol 3. 1st ed. New York, NY; Berlin Heidelberg/Germany: Springer-Verlag; 2000:53-116.

44. Seidelmann PK. *Explanatory Supplement to the Astronomical Almanac*. Mill Valley, CA: University Science Books; 1992.

45. Jezewski DJ. *Primer Vector Theory and Applications. Technical Report*. Houston, TX: National Aeronautics and Space Administration; Lyndon B. Johnson Space Center; 1975:77058.

46. Longo CRO, Rickman SL. *Method for the Calculation of Spacecraft Umbra and Penumbra Shadow Terminator Points. Technical Report. Technical Paper 3547*. NASA; 1995.

47. Betts JT. *Practical Methods for Optimal Control and Estimation Using Nonlinear Programming*. 2nd ed. Philadelphia, PA: Society for Industrial and Applied Mathematics; 2010.

APPENDIX A. CONSTANT PARAMETERS

Additional constants used in this research are defined as follows

$$\omega_\oplus = \frac{2\pi}{t_{\text{sid}}}, \tag{A1}$$

$$r_{\text{GEO}} = \sqrt[3]{\frac{\mu_\oplus}{\omega_\oplus^2}}, \tag{A2}$$

$$P_\odot = \frac{TSI}{c}, \tag{A3}$$

where $\omega_\oplus$ is Earth's angular velocity, r_{GEO} is the characteristic radius of a GEO, and $P_\odot$ is the ambient SRP at 1 AU.

Normalized units for distance (DU) and time (TU) are used for all numerical integration methods in this research and are designed such that the gravitational parameter is unity. Defining the distance unit equal to r_{GEO}, normalized units can be obtained as

$$1 \, DU = 42 \, 164.169637135361 \text{ km}$$
$$1 \, TU = 1371.344092645860 \text{ sec}$$
$$\therefore \mu_\oplus = 1 \, \frac{DU^3}{T}$$

TABLE A1 Physical parameters for celestial bodies

Body	Equatorial radius, R (km)	Gravitational parameter, $\mu \left(\frac{\text{km}^3}{\text{s}^2} \right)$
Earth ⊕	6378.1366	398 600.436233
Moon ☾	1737.4	4902.800076
Sun ☉	695 700	132 712 440 040.944000

TABLE A2   Physical constants

Parameter		Value	
Astronomical unit	AU	149 597 870.700	km
Total solar irradiance	TSI	1360.8	$\frac{W}{m^2}$
Speed of light	c	299 792.458	$\frac{km}{s}$
Solar day	t_{sol}	86 400	s
Sidereal day	t_{sid}	86 164.0905400	s
Gravitational coefficients	C_{20}	−1.08262617385222	10^{-3}
	C_{22}	1.57461532572292	10^{-6}
	S_{22}	−9.03872789196567	10^{-7}

APPENDIX B. INTER-AGENCY SPACE DEBRIS COORDINATION COMMITTEE GUIDELINES

Tables below provided from References 11,12.

TABLE B1   Protected GEO belt region

Orbit parameter	Definition
Radius	$r_{GEO} \pm 200$ km
Inclination	$\leq 15°$

Abbreviation: GEO, geostationary orbits.

TABLE B2   GEO region disposal guidelines

Orbit parameter	Definition	
Radius of perigee	$\leq r_{GEO} + 235$ km $+ \left(1000 \cdot C_R \cdot \frac{A}{m}\right)$	
	235 km:	Sum of the upper altitude of the GEO protected region (200 km) and the maximum descent of a reorbited spacecraft due to luni-solar and geopotential perturbations (35 km)
	C_R:	Solar radiation pressure coefficient (1 ~ 1.5)
	$\frac{A}{m}$:	Aspect area to dry mass $\left(\frac{m^2}{kg}\right)$
Eccentricity	≤ 0.003	

Abbreviation: GEO, geostationary orbits.